



Altenau, E. H., Pavelsky, T. M., Moller, D., Pitcher, L. H., Bates, P. D., Durand, M. T., & Smith, L. C. (2019). Temporal variations in river water surface elevation and slope captured by AirSWOT. *Remote Sensing of Environment*, 224, 304-316. <https://doi.org/10.1016/j.rse.2019.02.002>

Peer reviewed version

License (if available):
CC BY-NC-ND

Link to published version (if available):
[10.1016/j.rse.2019.02.002](https://doi.org/10.1016/j.rse.2019.02.002)

[Link to publication record in Explore Bristol Research](#)
PDF-document

This is the author accepted manuscript (AAM). The final published version (version of record) is available online via Elsevier at <https://www.sciencedirect.com/science/article/pii/S0034425719300495> . Please refer to any applicable terms of use of the publisher.

University of Bristol - Explore Bristol Research

General rights

This document is made available in accordance with publisher policies. Please cite only the published version using the reference above. Full terms of use are available: <http://www.bristol.ac.uk/pure/user-guides/explore-bristol-research/ebr-terms/>

1 **Temporal Variations in River Water Surface Elevation and Slope Captured by AirSWOT**

2
3 Elizabeth H. Altenau¹, Tamlin M. Pavelsky¹, Delwyn Moller², Lincoln H Pitcher³, Paul D.
4 Bates⁴, Michael T. Durand⁵, and Laurence C. Smith³

5
6 ¹Department of Geological Sciences, University of North Carolina, Chapel Hill, USA

7 ²Remote Sensing Solutions, Inc., Pasadena, CA, USA

8 ³Department of Geography, University of California, Los Angeles, USA

9 ⁴School of Geographical Sciences, University of Bristol, UK

10 ⁵School of Earth Science, and Byrd Polar and Climate Research Center, The Ohio State
11 University, Columbus, USA

12
13 **Corresponding Author:** Elizabeth Humphries Altenau (ealtenau@unc.edu)

14

15

16

17

18

19

20

21

22

23

24

25 **Abstract**

26 The Surface Water and Ocean Topography (SWOT) satellite mission aims to improve the
27 frequency and accuracy of global observations of river water surface elevations (WSEs) and
28 slopes. As part of the SWOT mission, an airborne analog, AirSWOT, provides spatially-
29 distributed measurements of WSEs for river reaches tens to hundreds of kilometers in length. For
30 the first time, we demonstrate the ability of AirSWOT to consistently measure temporal
31 dynamics in river WSE and slope. We evaluate data from six AirSWOT flights conducted
32 between June 7-22, 2015 along a ~90 km reach of the Tanana River, AK. To validate AirSWOT
33 measurements, we compare AirSWOT WSEs and slopes against an in situ network of 12
34 pressure transducers (PTs). Assuming error-free in situ data, AirSWOT measurements of river
35 WSEs have an overall root mean square difference (RMSD) of 11.8 cm when averaged over 1
36 km² areas whilst measurements of river surface slope have an RMSD of 1.6 cm/km for reach
37 lengths >5 km. AirSWOT is also capable of recording accurate river WSE changes between
38 flight dates, with an RMSD of 9.8 cm. Regrettably, observed in situ slope changes that transpired
39 between the six flights are well below AirSWOT's accuracy, limiting the evaluation of
40 AirSWOT's ability to capture temporal changes in slope. In addition to validating the direct
41 AirSWOT measurements, we compare discharge values calculated via Manning's equation using
42 AirSWOT WSEs and slopes to discharge values calculated using PT WSEs and slopes. We
43 define or calibrate the remaining discharge parameters using a combination of in situ and
44 remotely sensed observations, and we hold these remaining parameters constant between the two
45 types of calculations to evaluate the impact of using AirSWOT versus the PT observations of
46 WSE and slope. Results indicate that AirSWOT-derived discharge estimates are similar to the
47 PT-derived discharge estimates, with an RMSD of 13.8%. Additionally, 42% of the AirSWOT-

48 based discharge estimates fall within the PT discharge estimates' uncertainty bounds. We
49 conclude that AirSWOT can measure multitemporal variations in river WSE and spatial
50 variations in slope with both high accuracy and spatial sampling, providing a compelling
51 alternative to in situ measurements of regional-scale, spatiotemporal fluvial dynamics.

52 **1. Introduction**

53 The recent and rapid expansion of remote sensing technologies provides exciting
54 opportunities to address global-scale questions of fluvial process, especially in areas where in
55 situ observations are limited (Hannah et al., 2011; Pavelsky et al., 2014). Currently, the most
56 robust method for space-based observation of river water surface elevation (WSE) and slope is
57 satellite altimetry (Bates et al., 2014; Calmant et al., 2008; Tourian et al., 2016). A number of
58 studies use available altimeters to measure WSEs with accuracies ranging from 10 cm (ICESat,
59 SARAL/Altika) to several decimeters (TOPEX/Poseidon, Jason-2, Envisat) (Calmant et al.,
60 2008; O'Loughlin et al., 2016). These altimeter measurements have been used to validate flood
61 models, create time series of water level changes, estimate discharge, and quantify river height
62 and slope variability in inaccessible river basins (Domeneghetti, 2016; Garambois et al., 2016;
63 Kouraev et al., 2004; Papa et al., 2010; Paris et al., 2016; Tourian et al., 2016). However,
64 altimeter missions and their processing chains were primarily developed to measure sea surface
65 dynamics. As a result, altimeter observations of surface water bodies have complex error
66 characteristics due to variable waveforms, river or lake WSE changes within the altimeter
67 footprint, surrounding land elevations, and specular reflections (Alsdorf et al., 2007; Calmant et
68 al., 2008). Additionally, altimeters have low temporal (10-35 days) and spatial (70-600 m)
69 resolutions, along with large spatial gaps between orbital paths, which is not ideal for viewing
70 surface water dynamics. These characteristics limit the hydraulic visibility, the potential to

71 capture hydrological responses and hydraulic variabilities within a river network using remote
72 sensing, of the world's largest river systems to altimetry (Alsdorf et al., 2007; Calmant et al.,
73 2008; Garambois et al., 2016; Maillard et al., 2015; Smith, 1997).

74 The upcoming Surface Water and Ocean Topography (SWOT) mission plans to vastly
75 increase global observations of rivers 100 m wide and larger by providing 3-D measurements of
76 river WSEs from ~78°N to ~78°S (Biancamaria et al., 2016; Fjørtoft et al., 2014). SWOT's goal
77 is to measure river WSEs with an accuracy of 10 cm or better when averaged over 1 km² areas
78 and river surface slopes with an accuracy of 1.7 cm/km or better along 10 km reaches
79 (Rodriguez, 2016). As part of the SWOT mission, NASA has developed AirSWOT, an airborne
80 Ka-band interferometer that produces data products analogous to SWOT (Altenau et al., 2017b;
81 Biancamaria et al., 2016; Fu et al., 2015). AirSWOT is designed to measure high-accuracy
82 WSEs in a ~5 km wide swath that enables mapping of river reaches hundreds of kilometers in
83 length within a reasonable timeframe. Whilst there are some differences between AirSWOT's
84 incidence angles and planned SWOT viewing geometry, AirSWOT provides comparable
85 measurements to SWOT by recording elevations at the same radar wavelength (Ka-Band) and at
86 narrower incidence angles (~4-25°) than existing sensors. More detailed summaries of the
87 differences between AirSWOT and SWOT, along with AirSWOT's capabilities, are presented by
88 Moller et al. (2011) and Altenau et al. (2017b).

89 Previous work has shown that for a single day, AirSWOT can capture detailed spatial
90 variations in river WSEs and slopes with accuracies of 8-9 cm over 1 km² areas and 1-1.5 cm/km
91 over 10 km reaches. These results suggest that AirSWOT is capable of obtaining SWOT-like
92 measurements within the mission error requirements and is useful for understanding river
93 hydraulics at scales that will be unobservable by SWOT (Altenau et al., 2017b, Pitcher et al.,

94 2018). To date, however, AirSWOT has been tested against data from a single flight. The
95 ability of AirSWOT to accurately measure temporal variations in river WSEs and slopes remains
96 unknown. AirSWOT continues to be an experimental instrument with processing algorithms
97 under development. Furthermore, varying aircraft stability and roughness of the water surface
98 affect radar returns and impact AirSWOT's accuracy. Therefore, it is imperative to validate
99 AirSWOT measurements across and between collection days, in addition to the previously
100 published single-day results.

101 For the first time, we demonstrate the ability of AirSWOT to record river WSE and slope
102 changes between six different AirSWOT collections acquired over a three-week period.
103 Furthermore, we investigate the value of using AirSWOT measurements to estimate other
104 hydraulic quantities by comparing discharge calculated using AirSWOT WSEs and slopes versus
105 in situ WSEs and slopes, combined with other in situ and remotely sensed observations of depth
106 and width, in Manning's Equation.

107 **2. Study Site**

108 For this study, we conducted a six-week field campaign from May 15, 2015 to June 27,
109 2015 along a ~90 km reach of the Tanana River, Alaska, USA (Fig. 1a). This site is ideal for
110 assessment of AirSWOT's capabilities to measure WSEs and slopes over a highly-dynamic,
111 multichannel river offering challenges for AirSWOT beyond those of single-threaded, low relief
112 rivers. The shape of the annual hydrograph on the Tanana is dominated by melt of snowpack and
113 glaciers during the spring and summer. Mean annual discharge for the open-water season (May
114 to October) at the Nenana gauge station from 1962 to 2015 is ~1299 m³/s. The mean daily
115 discharge for the duration of the field campaign was 870 m³/s, which is very low for that time of
116 year. For comparison, the mean daily discharge for June 2016 was 1113 m³/s. There are three

117 primary tributaries that flow into the main study reach: Salchaket Slough, Chena River, and
118 Wood River. Based on the U.S. Geological stream gauges 15485500 Tanana River at Fairbanks,
119 AK and 15515500 Tanana River at Nenana, AK, these tributaries likely account for about ~20%
120 of the flow between the two gauge stations on average. The glacial origin of the Tanana River
121 results in a high sediment load, which interacts with local topography to produce a complex
122 morphology that ranges from highly braided to a single meandering channel (Brabets et al.,
123 2000). This varied river morphology, in combination with ubiquitous sandbars and high bluffs
124 (20-50 m high), makes the Tanana a challenging test site for AirSWOT's InSAR technology
125 (Altenau et al., 2017b).

126 **3. Methods**

127 **3.1 Field Measurements**

128 To validate AirSWOT measurements of river WSE and slope, we installed a network of
129 20 Solinst M5 Levelogger Edge pressure transducers (PTs) throughout the study reach to record
130 high-resolution, in situ measurements of changes in river height as well as two Solinst
131 Barologgers to compensate for atmospheric pressure fluctuations
132 (<https://www.solinst.com/products/data/3001.pdf>). Eight of the 20 pressure transducers are not
133 used in this study because they were buried by mobile sediment or riverbanks after installation as
134 a result of fluvial geomorphological processes. This left us with 12 viable pressure transducers to
135 calculate river height and slope changes (Fig. 1a). To deploy the PTs, we secured each device to
136 a cinderblock that was attached to the end of a long metal cable tethered to a fixed-point on the
137 bank of the river, usually a tree. We then placed the cinder block into the river about 5-10 m
138 from the bank. The distance between PTs ranged from 0.29-23 km, with the majority of the PTs
139 spaced 4-8 km apart. Data were recorded at 2 min intervals. Reported accuracy for the PTs is

140 ± 0.3 cm and ± 0.05 kPa (0.5 cm) for the Barologgers, resulting in a combined instrument
141 accuracy for water level measurements of ± 0.8 cm
142 (<https://www.solinst.com/products/data/3001.pdf>).

143 To convert the water depth measurements from the PTs to river WSEs, we used an
144 optical survey level to measure the height difference between the water surface and GPS
145 benchmarks (metal rods) that we placed near the fixed-point on the bank at each PT location. We
146 used the Canadian Spatial Reference System Precise Point Positioning tool (CSRS-PPP)
147 provided by Natural Resources Canada for static post-processing of the GPS surveys, providing
148 centimeter-level accuracies of the absolute WSEs collected at each PT site
149 (<http://www.nrcan.gc.ca/earth-sciences/geomatics/geodetic-reference-systems/>). The accuracy of
150 the GPS surveys ranges from ± 3.6 - 6.3 cm, while our optical survey accuracy is ± 0.2 cm,
151 bringing the total uncertainty for the PTs to ± 4.6 - 7.3 cm. It is also possible that the PTs
152 experienced some shifting or sinking due to the high mobility of the Tanana River bed (Brabets
153 et al., 2000). Any potential movements would add to the uncertainty in the PT WSEs. However,
154 we did not have robust methods for measuring these effects, therefore they are not accounted for
155 in our uncertainty calculations. A solid earth tide correction is accounted for in the AirSWOT
156 processing methodology, but not in the GPS post-processing. As a result, we apply a solid earth
157 tide correction to the PT WSE values using the program *solid*
158 (<http://geodesyworld.github.io/SOFTS/solid.htm#link0>).

159 In addition to the PTs, we collected a high-resolution GPS profile along the main channel
160 of the study reach on June 7, 2015 (Fig. 1a). We collected the profile using a Trimble R9 survey-
161 grade GPS system attached to the back of an 8.5 m river boat. GPS profile measurements were
162 post-processed using the CSRS-PPP tool in kinematic processing mode and provide nearly

163 continuous observations of river heights with ~3 m spacing between points and an uncertainty of
164 ± 2.0 cm in the vertical (Altenau et al., 2017b). Along with the river WSEs, we collected water
165 depths at each GPS profile point using a single-beam SonarMite Echo Sounder v.3.0. Instrument
166 accuracy for the echo sounder is ± 2.5 cm (<http://www.ohmex.com/sonarmite.html>).

167 **3.2 AirSWOT Measurements**

168 After installation of the PTs, six AirSWOT datasets were collected on June 7, June 9,
169 June 16, June 17, June 18, and June 22, 2015, to image temporal fluctuations in river WSE and
170 slope. Each AirSWOT mission consists of 4-24 overlapping flight lines per day, resulting in a
171 total of 66 individual lines of AirSWOT WSE measurements. The June 9th and June 16th
172 collections contain 24 flight lines covering a 43 km reach along the upstream portion of the field
173 site and a 32 km reach along the downstream portion of the field site, while the remaining flight
174 days each contain 4-6 flight lines of data covering the entire 90 km study reach (Fig. 1b-g).

175 The AirSWOT team at NASA's Jet Propulsion Laboratory processes the AirSWOT data
176 using custom software. Each AirSWOT flight line consists of 4 products, with the primary
177 product being the AirSWOT elevations measured in meters above the WGS84 ellipsoid. Other
178 products provided with the elevations are the relative radar backscatter (dB), incidence angle ($^{\circ}$)
179 and estimated elevation errors (m). Estimated elevation errors are calculated from the phase
180 variance (Cramer-Rao bound) which is based on the correlation between the two interferometric
181 images and depends on the sensor incidence angles, radar wavelength, and underlying surface
182 type (high topography, vegetation type, soil moisture, etc.) (Altenau et al., 2017b; Rosen et al.,
183 2000). All AirSWOT products are in a raster format and have a pixel resolution of 3.6 m in a
184 UTM 6N projection.

185 **3.3 2-D AirSWOT Filtering**

186 In this paper, we focus on the ability of AirSWOT to record changes in river WSEs and
187 slopes. To do so, we filter the 2-D AirSWOT measurements before spatially averaging and
188 comparing them to the PT surveys. Filtering the 2-D signal removes pixels containing WSE
189 outliers that are often due to layover and improper estimation of the ambiguity height parameter.
190 The ambiguity height is the amount of height change that leads to a 2π change in the
191 interferometric phase and is a key parameter in unwrapping the interferometric phase to calculate
192 elevation values (Rosen et al., 2000). When using near-nadir geometry, layover tends to occur in
193 environments with moderate-to-high topography, and the ambiguity heights have a faster range
194 variation (Neeck et al., 2012). As a result, calculating ambiguity heights can be more difficult,
195 especially in the near-swath and in areas adjacent to higher topography. Incorrect ambiguity
196 heights often lead to high vertical errors and geolocation errors in WSEs (Biancamaria et al.,
197 2016).

198 The first step in the filtering process is isolating the river pixels in the AirSWOT data.
199 For each AirSWOT line, we use a binary river mask created from a three-band color infrared
200 (CIR) camera (<http://cirrus-designs.com/>) on board the AirSWOT platform to isolate the river
201 pixels from surrounding land pixels. Regrettably, the majority of CIR images collected during
202 the AirSWOT flights were cloudy, which prevents us from using automatic methods to create an
203 independent river mask for each date. The CIR imagery were clear for the June 17th flight,
204 however, so we use these data to create a river mask and filter out the land pixels in each
205 AirSWOT line. We produce the river mask using a normalized difference water index (NDWI)
206 transformation with a threshold of 0.3 to identify water pixels (McFeeters, 1996). All pixels
207 greater than the threshold are assigned a value of one for water, and any pixels less than the
208 threshold are assigned a value of zero. Due to the high turbidity of the Tanana River, some

209 uncertainty in the water mask is introduced based on the chosen water threshold. As a result,
210 water pixels with high suspended sediment concentrations could be classified as land, or
211 conversely, land pixels that have NDWI values close to the chosen water threshold could be
212 classified as water. These misclassified pixels in the water mask could increase the noise in the
213 identified AirSWOT WSE pixels. Additionally, the river on June 17th was at a lower stage than
214 the majority of the data collections with the exception of June 16th, which had a stage about 5 cm
215 lower than June 17th. Therefore, the river extent observed in the river mask should be comparable
216 to June 16th, but is likely to exclude some inundated pixels on the other collection days.

217 Once the river WSEs are isolated, we use a 2 km² moving window to remove extreme
218 outliers by erasing pixels ± 3 standard deviations away from the mean river WSE in the window
219 (Altenau et al., 2017b). This filter helps eliminate pixels affected by layover from adjacent high
220 topography and vegetation, as well as misclassified water/land pixels from the water mask.
221 Despite the initial outlier filter, there are some large areas affected by ambiguity height errors
222 that are not removed during the filtering process because they significantly affect the statistics
223 within the 2 km² window. Therefore, we manually remove the incorrect pixels in these areas
224 (Fig. 2). These larger areas of ambiguity height errors are prominent in 9 of the 66 AirSWOT
225 lines. Fig. 3a shows the effects of the 2-D filtering process on the distribution of WSEs for all the
226 AirSWOT flights. Overall, ~95% of the pixels are retained during the initial 2-D filtering.

227 **3.4 WSE Validation**

228 After filtering the 2-D AirSWOT measurements, we spatially average the WSEs and
229 slopes before comparing AirSWOT to the PT observations. Spatial averaging is commonly
230 applied to interferometric measurements in order to reduce random errors that are independent
231 from pixel to pixel (Rodriguez and Martin, 1992). The SWOT mission accuracy requirement for

232 river WSEs of 10 cm is based on averaging pixels within 1 km² areas, a threshold the SWOT
233 Science Team has determined will allow significant scientific advances in fluvial hydrology
234 (Rodriguez, 2016). Therefore, we use this area requirement as a baseline for assessing
235 AirSWOT's capabilities for capturing same-day river WSEs as well as their changes over time
236 (Altenau et al., 2017b). To quantify WSE differences between AirSWOT and the in situ
237 measurements for each flight date, we calculate a weighted average of the filtered AirSWOT
238 WSEs within 1 km² areas around each PT using the following equation:

239

$$\bar{x} = \frac{\sum_{i=1}^n x_i w_i}{\sum_{i=1}^n w_i} \quad (1)$$

240 where \bar{x} is the weighted average of the AirSWOT WSEs at a single PT location, x_i is the
241 AirSWOT WSE for each pixel (i), and w_i is the weight associated with each pixel and is
242 determined by AirSWOT's estimated elevation error (e_i , see Section 3.2):

$$w_i = \frac{1}{e_i^2} \quad (2)$$

243 As a result, pixels with lower estimated errors have more influence in the final weighted average
244 than the pixels with larger estimated errors.

245 Despite the initial 2-D filtering of the AirSWOT WSEs, some remaining erroneous pixels
246 affected by ambiguity height errors are still present in the data. These pixels tend to have large
247 vertical offsets compared to field observations but low e_i values, resulting in comparatively high
248 errors in the weighted average calculation. To reduce the effects of these pixels, we calculate the
249 median for each 1 km² area and retain 70% of the AirSWOT WSEs that surround the median
250 value. We also eliminate pixels that have estimated errors of < 0.1 m because we find these
251 particularly low error estimates often correspond with pixels that are affected by ambiguity

252 height errors. Pixels with estimated errors < 0.1 m make up less than 1% of the data, therefore
253 this second filter preserves about 70% of the data within each 1 km^2 area while reducing the
254 errors in the weighted average that are caused by the incorrect pixels. The spatial filtering within
255 the 1 km^2 areas and application of the weighted mean reduces the mean average difference
256 (MAD) between AirSWOT and PT WSEs by 68% compared to calculating a simple mean on the
257 unfiltered data (Fig. 3b).

258 It is difficult to calculate uncertainties for the averaged WSEs using the AirSWOT data
259 alone. We can calculate the random error component of the uncertainty for the averaged
260 AirSWOT WSEs based on the weights (w_i):

$$uncertainty = \frac{\sqrt{F}}{\sqrt{\sum_{i=1}^n w_i}} \quad (3)$$

261 where F is a factor that accounts for the oversampling of pixels within the gridded UTM product
262 relative to the sampling assumed when estimating the elevation errors. F depends on the
263 incidence angle (I):

$$F = \frac{0.52}{\sin(I)} \quad (4)$$

264 The constant 0.52 comes from the ratio $(1.87 \text{ m})/(3.6 \text{ m})$ where 1.87 m is the effective spatial
265 resolution for 80 MHz bandwidth and 3.6 m is the UTM posting. Equation 3 accounts for the
266 random error component (noise on the interferometric phase) in the AirSWOT measurement
267 uncertainty, but does not include systematic errors that are due to variations in antenna pointing
268 and incomplete knowledge of the airborne platform location such as attitude errors, baseline
269 errors, and position errors (Rodriguez and Martin, 1992; Rosen et al., 2000). As a result, the
270 uncertainties calculated using equation 3, which range from 0.1 – 2.0 cm, only account for a

271 small fraction of the total error and are unrealistically low. Systematic errors in the AirSWOT
272 data affect the accuracy of the WSEs, and likely add to the random error uncertainty, but cannot
273 be quantified from the data itself or from available ancillary information. Rather than present
274 misleading uncertainty values, we elect to not designate uncertainties for the averaged AirSWOT
275 WSEs, and focus instead on reporting observed differences between the AirSWOT and PT
276 measurements, as this comparison provides an empirical estimate of the total error.

277 Once the averaged AirSWOT WSEs are determined, we calculate the same-day, absolute
278 differences and associated root-mean-square differences (RMSDs) between the AirSWOT and
279 PT WSEs. Although Altenau et al. (2017b) report no bias in the June 9th AirSWOT
280 measurements along the Tanana River, we observe a spatially consistent negative bias across the
281 AirSWOT WSEs that ranges from -8 cm to -20 cm depending on the collection day. The
282 AirSWOT data presented in this paper are processed using different methods from the data
283 presented in Altenau et al. (2017b), and we have not determined the source of the bias in the
284 current data at this time. Possible explanations for the bias include improper common range
285 calibrations, differences in how solid earth tide corrections are incorporated, erroneous GPS
286 solutions, and problems with the troposphere correction. As a result, we subtract the mean bias
287 on each day from the AirSWOT WSEs and recalculate the absolute differences and RMSDs
288 between the same-day, bias-corrected AirSWOT measurements and PT WSEs (Table 1).

289 In addition to the same-day WSEs, we calculate WSE change values for the PTs and bias-
290 corrected AirSWOT measurements between the first AirSWOT date (June 7th) and all
291 subsequent dates ($n = 58$), as well as WSE changes between all possible AirSWOT date
292 combinations ($n = 161$). We estimate uncertainties for the PT WSE changes by taking the root
293 sum of squares of the uncertainties in the daily PT WSEs. Finally, we calculate the absolute

294 differences and RMSDs between the bias-corrected AirSWOT and PT WSE change
295 observations.

296 **3.5 Slope Validation**

297 Using different combinations of the 12 PT locations, we identify a total of 63 pairs of PT
298 sites (e.g. PT01 and PT05) for calculating along-flow river surface slopes with reach lengths
299 between PT points ranging from 5.1 to 83.6 km. At reach lengths <5 km AirSWOT slopes
300 become severely affected by high-variability noise likely resulting from layover and ambiguity
301 height errors. Therefore, PT combinations with reach lengths <5 km are not included here. For
302 each PT pair, we calculate the PT surface slopes by dividing the difference in WSE by the reach
303 length between the PT sites.

304 To compare the PT slopes to AirSWOT slopes, we first create 1-D, high-resolution
305 AirSWOT profiles by extracting the 2-D AirSWOT WSE measurements coincident to the GPS
306 profile locations collected in the field (Fig. 1a). At each GPS profile point, we calculate a 1 km
307 orthogonal vector across the Tanana River and use equation 3.1 to calculate a weighted mean of
308 the 2-D AirSWOT WSEs along the orthogonal vector. After the weighted averaging, we create
309 the final 1-D AirSWOT profiles by applying a running median filter with a window of 500 pixels
310 (~1600 m) to eliminate large peaks in the initial profiles (Fig. 4). The running median filter
311 reduces high frequency variability, which is unrealistic for a large river like the Tanana. We
312 validate the running median filter by comparing the initial profile and filtered profile on June 7th
313 to the GPS profile WSEs that were also collected on June 7th. When compared to the GPS
314 profile, applying the running median filter reduces the final AirSWOT profile RMSD to 18.6 cm
315 versus 69.3 cm for the initial AirSWOT profile (Fig. 5). While a window size of 500 pixels
316 works well for the Tanana River profile, optimal window size will likely vary among river

317 environments depending on topography, morphology, size, and other factors. Currently,
318 knowledge about the field site, or in situ observations, are required to determine the optimal
319 window size for smoothing. However, future measurements from the SWOT satellite mission
320 will provide river WSE profiles with higher accuracies than existing digital elevation models
321 (Langhorst et al., unpublished results), which will aid in applying this methodology to ungauged
322 or hard to access rivers.

323 Once the 1-D WSE profiles are created, we use ordinary least squares linear regressions
324 to calculate same-day slopes along the AirSWOT profiles between each of the 63 PT pair
325 locations. We estimate AirSWOT slope uncertainties using the linear regressions, and the PT
326 slope uncertainties by calculating the difference between the maximum and minimum slopes for
327 each PT pair, which are based on the PT WSE uncertainties. To validate AirSWOT slope
328 measurements, we calculate absolute differences and RMSDs between the same-day AirSWOT
329 and PT slopes (Table 1). Due to equipment constraints, we do not have high-resolution GPS
330 profiles along the study reach for each separate AirSWOT flight and are limited to validating
331 temporal fluctuations in AirSWOT slopes against the PT observations. Therefore, we use linear
332 regressions to calculate AirSWOT slopes over more sophisticated methods, such as LOESS
333 filters, because we cannot validate spatial variations in AirSWOT slopes against the PT
334 measurements. Altenau et al. (2017b) present results regarding AirSWOT's ability to capture
335 detailed spatial variations in WSE and slope along the same study reach of the Tanana River.

336 Next, we calculate the slope changes between the first AirSWOT date (June 7th) and all
337 subsequent dates ($n = 297$), as well as all possible AirSWOT date combinations ($n = 766$). To
338 estimate uncertainties for the slope changes, we take the root sum of squares of the uncertainties
339 in the same-day PT and AirSWOT slopes. We then calculate absolute differences for the

340 AirSWOT and PT slope changes between June 7th and all subsequent dates, and slope changes
341 between all possible date combinations.

342 **3.6 Discharge Estimation**

343 In addition to validating AirSWOT's ability to capture temporal fluctuations in river
344 WSE and slope, we assess how AirSWOT observations compare to PT observations of WSE and
345 slope when calculating discharge at each PT location using Manning's equation (Manning et al.,
346 1890):

$$Q = \frac{1}{n} AR^{2/3} \sqrt{S} \quad (5)$$

347 where Q is the discharge, A is the cross sectional area, R is the hydraulic radius, S is the river
348 surface slope, and n is Manning's roughness coefficient.

349 First, we estimate the cross sectional area at each PT location. To derive depths, we use
350 the bathymetric measurements collected with the echo sounder (see Section 3.1) to identify the
351 average river bed elevation, or lowest point in a cross section, at each PT location. The bed
352 elevation measurements were collected independently of the PT measurements and stay constant
353 in time at each PT site. We derive the temporally-varying depth values used to calculate the cross
354 sectional area at each PT site by subtracting the static bed elevations from the temporally varying
355 PT and AirSWOT WSEs (Altenau et al., 2017a).

356 For cross sectional widths, we use the CIR imagery collected during each AirSWOT
357 flight to manually measure the river widths at the various PT sites on each day, since the clouds
358 in the imagery inhibit us from using automatic width detection methods. Two PTs lack width
359 measurements for several days due to dense cloud cover (PT07) and fewer AirSWOT
360 observations (PT10). Therefore, we exclude these PTs in the discharge estimation, leaving us ten
361 PT locations to calculate discharge. To test the effect of channel geometry on the calculated

362 discharge values, we perform a sensitivity analysis for 4 different cross sectional shapes
363 (rectangle, parabola, triangle, and trapezoid). For the trapezoidal cross section, we assume the
364 base width is half the top width. We find a negligible (0.2%) effect on mean discharge
365 differences between cross sectional shapes, therefore, we use a simple rectangular geometry to
366 calculate cross sectional area by multiplying the river width by depth.

367 Next, we estimate the river surface slope at each cross section by locating the closest
368 upstream and downstream PTs to the current PT location and calculating the slope between the
369 two bounding sites. The two exceptions are the first and last PT locations #1 (PT01) and #12
370 (PT12) for which we use the closest downstream and upstream location only to calculate the
371 slopes. For example, we determine the slope for PT05 by calculating the slope between PT04
372 and PT06, and we determine PT01's slope by calculating the slope between PT01 and PT02.

373 Finally, we calibrate temporally-varying roughness coefficients at each PT site by
374 calculating PT discharge estimates over a range of roughness values (0.01-0.1) and comparing
375 the estimates to in situ discharge values from the Nenana gauge station at the downstream end of
376 the study reach (Fig. 1a, Table 2). We assess how well AirSWOT measurements compare to the
377 PT measurements of WSE and slope when estimating discharge by calculating daily and overall
378 RMSD values between the PT and AirSWOT discharge values. The goal in this analysis is to
379 compare discharge values calculated using AirSWOT measurements of WSE and slope to
380 discharge values calculated using the PT measurements of WSE and slope, holding all other
381 variables constant, not to invert discharge values using mass conserved flow law inversion
382 methods like those discussed by Durand et al. (2016). Because we calibrate Manning's n to the
383 gauge station discharge, the discharge values we calculate are not independent of the gauge, and
384 we do not attempt to compare the discharge estimates to the gauge observations or analyze the

385 effects of tributary inputs at the different PT locations. We do, however, display the Nenana
386 gauge discharge values for reference.

387 **4. Results**

388 Spatial patterns and biases in the differences between the same-day AirSWOT and PT
389 WSEs are similar across all days, which indicates the separate AirSWOT flights are affected by
390 comparable error sources (Fig. 6a,c; Table 1). RMSDs for the same-day, bias-corrected
391 AirSWOT WSEs range from 8.3 cm to 15.0 cm with an overall RMSD of 11.8 cm. The
392 consistency in the same-day AirSWOT WSE differences and biases allows AirSWOT to capture
393 the same general pattern in temporal WSE changes as the PTs, with an RMSD of 9.8 cm for all
394 possible date combinations (Fig. 7). Had the same-day WSE differences shown variable patterns
395 and bias directions for each AirSWOT flight, high-accuracy WSE changes would be less
396 detectable. Between the different PT locations, AirSWOT WSE change differences shift from
397 underestimations upstream to overestimations downstream (Fig. 7c). The variations in WSE
398 change differences between the PT sites are likely due to the different environmental conditions
399 at each location and how they affect the radar returns. High topography, water surface roughness,
400 width and number of channels in a cross section, and bare versus vegetated banks all influence
401 the strength and quality of the radar returns at a specific PT location. For example, PT10 displays
402 a comparatively large range in WSE change differences (Fig. 7c). PT10 is directly adjacent to an
403 area of high topography, making it susceptible to layover errors, and is not covered by the high
404 observational density June 9th and June 16th AirSWOT collections, leaving only data collections
405 with fewer observations in the calculation of WSE changes.

406 In addition to the WSEs, AirSWOT is able to measure river surface slopes with an
407 RMSD of 1.6 cm/km, and 98% of slope differences fall below 3.0 cm/km for reach lengths ≥ 5

408 km (Table 1, Fig. 6d). Same-day slope differences increase as reach length decreases.
409 Unfortunately, the Tanana River slopes do not significantly change between the six AirSWOT
410 collection days, though slight increases in slope, within the margin of error, are observed by the
411 PTs as stage decreases (Fig. 8a). Mean slope changes observed by the PTs from June 7th to all
412 subsequent dates ranged from 0.07 cm/km to 0.17 cm/km. These observed slope changes are
413 well below AirSWOT's slope accuracy, but variations in mean AirSWOT slope change are
414 similarly low, ranging from -0.35 cm/km to 0.26 cm/km (Fig. 8a). Additionally, AirSWOT
415 displays lower slope uncertainties than the PTs due to the high spatial density of the AirSWOT
416 measurements with slope uncertainties decreasing exponentially as reach length increases (Fig.
417 8b).

418 Both PT and AirSWOT discharge estimates capture the general hydrograph pattern
419 observed by the Nenana gauge station, with discharge decreasing until June 16th and increasing
420 thereafter (Fig. 9). AirSWOT discharge values display a 13.8% difference compared to the PT
421 values, on average, with RMSDs ranging from 11.1% to 18.0% (Table 3). 42% of the AirSWOT
422 discharge estimates fall within the PT discharge uncertainty bounds. Discharge differences are
423 predominately related to the AirSWOT WSE differences. A linear regression between discharge
424 differences and WSE differences ($R^2=0.88$) shows a 1.1% increase in discharge difference with
425 every centimeter of WSE difference (Fig. 10a). Conversely, there is no statistically significant
426 relationship between AirSWOT slope differences and discharge differences, with an $R^2=0.03$
427 (Fig. 10b).

428 **5. Discussion and Conclusion**

429 In this study, we present a first analysis of AirSWOT's ability to observe temporal
430 variations in river WSE and slope over variable reach lengths and timescales. Altenau et al.

431 (2017b) and Pitcher et al. (2018) document AirSWOT's ability to record accurate river WSEs
432 and slopes for one collection date, while here we analyze the consistency of AirSWOT
433 measurements over the course of three weeks and six different flights. It is not always
434 straightforward for AirSWOT to measure same-day river WSEs due to errors and biases likely
435 related to the movement of the aircraft, variations in water surface roughness, and difficulties in
436 phase unwrapping at narrower incidence angles ($<5^\circ$) (Biancamaria et al., 2016, Neeck et al.,
437 2012). Comparisons with PT observations illustrate that AirSWOT accurately captures temporal
438 water surface fluctuations along a complex, anabranching river system, with an RMSD of 11.8
439 cm for same-day WSEs (Fig. 6c., Table 2). Given the differences between the PT and AirSWOT
440 same-day WSEs display consistent patterns between flight collections, AirSWOT is also able to
441 capture decimeter-level WSE changes, with an RMSD of 9.8 cm for all possible date
442 combinations (Fig. 7c). Some of the differences between the AirSWOT and the PT WSEs could
443 be due to the spatial averaging of the AirSWOT data or the PT uncertainty (± 4.6 - 7.3 cm), which
444 is a result of the instrument and GPS survey errors. PTs provide WSE measurements at a specific
445 location in the cross section. Due to superelevation, the PTs could record different WSE values
446 depending on whether they were placed on the inside or outside of a meander bend. These cross-
447 sectional effects on WSE would be observable by PTs if they were placed appropriately in the
448 channel, but they are below the accuracy of the 2-D AirSWOT signal. Averaging over 1 km^2
449 areas, which is required to achieve decimeter-level accuracies in the AirSWOT WSEs, also
450 results in averaging out any superelevation signal.

451 In contrast to river WSEs, AirSWOT is capable of producing robust river surface slope
452 measurements with an RMSD of 1.6 cm/km for same-day slopes for reach lengths ≥ 5 km (Table
453 2). While the slope changes observed along the Tanana River are significantly smaller than

454 AirSWOT's daily slope accuracy, it is important to note that AirSWOT does detect extremely
455 low temporal variability in slopes similar to the PT measurements (Fig. 8a). This low slope
456 variability over time is somewhat surprising considering the dip in the hydrograph that occurs
457 during the measurement period (Fig. 1a). We suggest several possible explanations for the low
458 temporal variability in slopes along the Tanana River: (1) The rate of discharge change is
459 actually quite low ($\pm 30 \text{ m}^3/\text{s}/\text{day}$) compared to the rates of change associated with snowmelt and
460 rainfall hydrographs moving through this reach of the Tanana. As a result, the 'wave' generated
461 by this discharge change has relatively low amplitude and varies more gradually than is typical
462 for this system. (2) Surface water slopes along this river reach may have strong 'base level
463 control' by width constrictions due to the adjacent high bluffs and geologic setting. (3) There is
464 some evidence that temporal variability in water slope is low for other anabranching river
465 systems. For example, O'Loughlin et al. (2013) found only $\sim 0.15 \text{ cm}/\text{km}$ of slope change
466 between the falling and rising limbs of the hydrograph along the middle reach of the Congo
467 River. Additional research is needed during more extreme hydrologic events, or along rivers with
468 larger slope variability over time, in order to draw definitive conclusions regarding AirSWOT's
469 accuracy in observing temporal slope changes.

470 In addition to validating AirSWOT's direct measurements of river WSE and slope, we
471 test the effectiveness of the AirSWOT observations for approximating discharge compared to the
472 PT observations. To do so, we use Manning's equation to calculate and compare discharge
473 values using both the PT and AirSWOT measurements of river WSE and slope. We hold the
474 other discharge parameters constant between the PT and AirSWOT calculations, and derive them
475 from additional in situ (depth, Manning's n) and remotely sensed observations (width).
476 Discharge estimates calculated using AirSWOT measurements of WSE and slope result in

477 marginal differences compared to discharge estimates calculated using the PT observations of
478 WSE and slope. On average, AirSWOT discharge estimates are within 13.8% of the estimates
479 attained using the PTs, and 42% of the time AirSWOT discharge measurements fall within the
480 PT discharge uncertainty (Table 3). For the Tanana River, AirSWOT WSE differences dominate
481 the observed discharge differences, with slope differences showing little effect (Fig. 10). This
482 result is likely due, in part, to the limited slope variations occurring throughout the Tanana River
483 during the field campaign. Because development of AirSWOT processing methods is ongoing,
484 AirSWOT WSE errors and biases are likely to decrease in the future, along with a corresponding
485 decrease in discharge errors. When combined with sophisticated algorithms and appropriate
486 parameters, AirSWOT measurements can be used to invert discharge fluctuations along
487 inaccessible and unmonitored river networks (Bjerklie et al., 2005; Bonnema et al., 2016;
488 Durand et al., 2016; Hagemann et al., 2017), potentially including rivers that are too small to
489 observe using satellite sensors yet have important biogeochemical and ecological impacts (Allen
490 and Pavelsky, 2018; King et al., 2018).

491 Despite the challenges inherent in making precise measurements of WSEs when using an
492 airborne radar, AirSWOT provides a compelling alternative to current remote sensing and in situ
493 observations for measuring river dynamics. AirSWOT's slope measurements are particularly
494 notable due to their high accuracy and spatial density. In situ river gauging stations, or pressure
495 transducers, provide accurate WSE measurements at one location, but are not ideal for estimating
496 slope variability along river reaches due to their coarse spatial coverage. For example, gauge
497 stations are typically spaced tens to hundreds of kilometers apart and have limited placement
498 options due to equipment functionality and accessibility constraints (Allen and Pavelsky, 2015;
499 Bates, 2004; Hannah et al., 2011). In addition to in situ methods, studies using nadir altimeter

500 data to estimate river slopes contend with poor spatial resolutions, wide track spacings between
501 observations, and significant height uncertainties (Garambois et al., 2016; O’Loughlin et al.,
502 2013, 2016). In contrast, AirSWOT can provide spatially distributed measurements of WSE
503 along hundreds of kilometers of river, which can capture detailed spatial variabilities in river
504 WSEs and provide better-constrained slope estimates compared to in situ sensors and satellite
505 altimeters (Altenau et al., 2017b).

506 In addition to spaceborne observations, alternative airborne sensors insufficiently
507 measure river WSEs and slopes. Specifically, airborne LiDAR systems, which are known for
508 their high-accuracy measurements of land surfaces, tend to provide poorer returns over open
509 water surfaces due to the absorption of the laser beam within the water column, low signal-to-
510 noise ratios, and high occurrences of specular reflection (Antonarakis et al., 2008; Sanders, 2007;
511 Schumann et al., 2008; Smith et al., 2009). As a result, most studies that utilize LiDAR
512 measurements over inland waters focus on classifying water body areas not WSE or slope
513 (Antonarakis et al., 2008; Crasto et al., 2015; Höfle, 2009). Recently, Branch et al. (2018) and
514 Hudson et al. (2017) used airborne LiDAR transects to map river WSEs and slopes along the
515 Columbia River Estuary. They found spatially-averaged LiDAR WSEs agreed with a local tide
516 gauge to within an RMSE of ~40 cm, but had difficulty deriving precise slope estimates from the
517 LiDAR data due to under sampling and sampling error. These results suggest AirSWOT provides
518 superior measurements of river WSEs and slope compared to alternative LiDAR systems.

519 Though AirSWOT data is not available globally, it presents an opportunity to study
520 regional hydraulics and hydrology in novel ways (Altenau et al., 2017b; Pitcher et al., 2018).
521 Current and future projects combine AirSWOT observations with other spaceborne and airborne
522 sensors including LiDAR, multispectral, and hyperspectral imagers to study interactions between

523 surface water dynamics, geochemical fluxes, and geomorphic processes. The Arctic-Boreal
524 Vulnerability Experiment (AboVE) (<https://above.nasa.gov/about.html>), ongoing, combines in
525 situ observations including WSE, methane, and CO₂ with remotely sensed data products of WSE
526 (AirSWOT), soil moisture, and water quality to better understand the fast changing ecosystem
527 dynamics in arctic and boreal regions. Additionally, the recently funded Delta-X project plans to
528 combine in situ data, model outputs, and remote sensing observations from a variety of airborne
529 sensors, including AirSWOT, to improve current understanding of water partitioning and
530 sedimentation dynamics in the Mississippi River Delta. Furthermore, measurements of river
531 WSEs and slopes from AirSWOT can be used for calibration, validation, and assimilation into
532 local and regional-scale flood models to improve their performance by providing similar, and
533 often superior, accuracies and better spatiotemporal coverage than existing airborne and satellite
534 sensors. Finally, results from this study and others indicate AirSWOT accuracies consistently
535 meet the SWOT mission accuracy requirements for river processes (Altenau et al., 2017b,
536 Pitcher et al., 2018), which suggests AirSWOT could be a valuable tool for validating future
537 SWOT measurements of river WSE and slope in complex and hard to reach river basins with
538 little in situ data.

539 **Acknowledgements**

540 This work was funded by NASA Terrestrial Hydrology Program Grant # NNX13AD05G,
541 managed by Jared Entin. Field locations and observations of water surface elevation were based
542 on equipment services provided by the UNAVCO Facility with support from the National
543 Science Foundation (NSF) and National Aeronautics and Space Administration (NASA) under
544 NSF Cooperative Agreement No. EAR-0735156. Laurence C. Smith acknowledges additional
545 support from NASA #NNX16AH85G and Paul D. Bates is supported by a Leverhulme Research

546 Fellowship and a Royal Society Wolfson Research Merit award. We acknowledge Curtis Chen,
547 Craig Stringham, Albert Chen, Xiaaoqing Wu, Gregory Sadowy, and the JPL AFRC AirSWOT
548 teams for collection and processing of the AirSWOT data, as well as John Arvesen from Cirrus
549 Digital Systems for processing the CIR imagery. We also want to thank our boat driver Sam
550 Demientieff for his navigational expertise on the Tanana River, which allowed for safe and
551 timely data collection. Finally, we would like to thank the three anonymous reviewers who
552 provided comments that helped improve the quality of the manuscript. All of the data in the main
553 text are presented in the figures and may be obtained from Elizabeth H. Altenau (email:
554 ealtenau@unc.edu).

REFERENCES

- 555
556
557 Allen, G.H., Pavelsky, T., 2018. Global extent of rivers and streams. *Science* (80-.). 361, 585–
558 588. <https://doi.org/10.1126/science.aat063>
- 559 Allen, G.H., Pavelsky, T.M., 2015. Patterns of river width and surface area newly revealed by
560 the satellite-derived North American River Width (NARWidth) dataset. *Geophys. Res. Lett.*
561 1–14. <https://doi.org/10.1002/2014GL062764>.Received
- 562 Alsdorf, D.E., Rodríguez, E., Lettenmaier, D.P., 2007. Measuring surface water from space. *Rev.*
563 *Geophys.* 45, RG2002. <https://doi.org/10.1029/2006RG000197>
- 564 Altenau, E.H., Pavelsky, T.M., Bates, P.D., Neal, J.C., 2017a. The effects of spatial resolution
565 and dimensionality on modeling regional-scale hydraulics in a multichannel river. *Water*
566 *Resour. Res.* 53, 1683–1701. <https://doi.org/10.1002/2016WR019396>
- 567 Altenau, E.H., Pavelsky, T.M., Moller, D., Lion, C., Pitcher, L.H., Allen, G.H., Bates, P.D.,
568 Calmant, S., Durand, M., Smith, L.C., 2017b. AirSWOT measurements of river water
569 surface elevation and slope: Tanana River, AK. *Geophys. Res. Lett.* 1–9.
570 <https://doi.org/10.1002/2016GL071577>
- 571 Antonarakis, A.S., Richards, K.S., Brasington, J., 2008. Object-based land cover classification
572 using airborne LiDAR. *Remote Sens. Environ.* 112, 2988–2998.
573 <https://doi.org/10.1016/j.rse.2008.02.004>
- 574 Bates, P.D., 2004. Remote sensing and flood inundation modelling. *Hydrol. Process.* 18, 2593–
575 2597. <https://doi.org/10.1002/hyp.5649>
- 576 Bates, P.D., Neal, J.C., Alsdorf, D., Schumann, G.J.-P., 2014. Observing Global Surface Water
577 Flood Dynamics. *Surv. Geophys.* 35, 839–852. <https://doi.org/10.1007/s10712-013-9269-4>
- 578 Biancamaria, S., Lettenmaier, D.P., Pavelsky, T.M., 2016. The SWOT Mission and Its
579 Capabilities for Land Hydrology. *Surv. Geophys.* 37, 307–337.
580 <https://doi.org/10.1007/s10712-015-9346-y>
- 581 Bjerklie, D.M., Moller, D., Smith, L.C., Dingman, S.L., 2005. Estimating discharge in rivers
582 using remotely sensed hydraulic information. *J. Hydrol.* 309, 191–209.
583 <https://doi.org/10.1016/j.jhydrol.2004.11.022>
- 584 Bonnema, M.G., Sikder, S., Hossain, F., Durand, M., Gleason, C., Bjerklie, D.M., 2016.
585 Benchmarking wide swath altimetry-based river discharge estimation algorithms for the
586 Ganges river system. *Water Resour. Res.* 52, 5974–5997.
587 <https://doi.org/10.1002/2016WR018977>.Received
- 588 Brabets, T.P., Wang, B., Meade, R.H., 2000. Environmental and Hydrologic Overview of the
589 Yukon River Basin , Alaska and Canada. US Dep. Inter. US Geol. Surv.
- 590 Branch, R.A., Horner-Devine, A.R., Akan, C., Chickadel, C.C., Farquharson, G., Hudson, A.,
591 Talke, S.A., Thomson, J., Jessup, A.T., 2018. Airborne LiDAR Measurements and Model
592 Simulations of Tides, Waves, and Surface Slope at the Mouth of the Columbia River. *IEEE*
593 *Trans. Geosci. Remote Sens.* 56, 7038–7048. <https://doi.org/10.1109/TGRS.2018.2847561>
- 594 Calmant, S., Seyler, F., Cretaux, J.F., 2008. Monitoring continental surface waters by satellite
595 altimetry. *Surv. Geophys.* 29, 247–269. <https://doi.org/10.1007/s10712-008-9051-1>
- 596 Crasto, N., Hopkinson, C., Forbes, D.L., Lesack, L., Marsh, P., Spooner, I., van der Sanden, J.J.,
597 2015. A LiDAR-based decision-tree classification of open water surfaces in an Arctic delta.
598 *Remote Sens. Environ.* 164, 90–102. <https://doi.org/10.1016/j.rse.2015.04.011>
- 599 Domeneghetti, A., 2016. On the use of SRTM and altimetry data for flood modeling in data-
600 sparse regions. *Water Resour. Res.* 1–20. <https://doi.org/10.1002/2014WR015716>

601 Durand, M., Gleason, C., Garambois, P.A., Bjerklie, D., Smith, L.C., Roux, H., Rodríguez, E.,
602 Bates, P.D., Pavelsky, T.M., Monnier, J., Chen, X., Di Baldassarre, G., Fiset, J.-M., Flipo,
603 N., Frasson, R.P. de M., Fulton, J., Goutal, N., Hossain, F., Humphries, E., Minear, J.T.,
604 Mukolwe, M.M., Neal, J.C., Ricci, S., Sanders, B.F., Schumann, G., Schubert, J.E., Vilmin,
605 L., 2016. An intercomparison of remote sensing river discharge estimation algorithms
606 from measurements of river height, width, and slope. *Water Resour. Res.* 52, 613–615.
607 <https://doi.org/10.1029/2008WR006912>

608 Fjørtoft, R., Gaudin, J.M., Pourthié, N., Lalaurie, J.C., Mallet, A., Nouvel, J.F., Martinot-
609 Lagarde, J., Oriot, H., Borderies, P., Ruiz, C., Daniel, S., 2014. KaRIn on SWOT:
610 Characteristics of near-nadir Ka-band interferometric SAR imagery. *IEEE Trans. Geosci.*
611 *Remote Sens.* 52, 2172–2185. <https://doi.org/10.1109/TGRS.2013.2258402>

612 Fu, L.-L., Alsdorf, D., Morrow, R., Rodriguez, E., 2015. SWOT: The Surface Water and Ocean
613 Topography Mission. SWOT NASA/JPL Proj.
614 <https://doi.org/10.1017/CBO9781107415324.004>

615 Garambois, P., Calmant, S., Roux, H., Paris, A., Finaud-guyot, P., Montazem, A., Santos, J.,
616 Spatales, O., Cnes, U.M.R., Ird, C., 2016. Hydraulic visibility : using satellite altimetry to
617 parameterize a hydraulic model of an ungauged reach of a braided river. *Hydrol. Process.*
618 30, 1–20. <https://doi.org/10.1002/hyp.11033>

619 Hagemann, M.W., Gleason, C.J., Durand, M.T., 2017. BAM: Bayesian AMHG-Manning
620 Inference of Discharge Using Remotely Sensed Stream Width, Slope, and Height. *Water*
621 *Resour. Res.* 53, 9692–9707. <https://doi.org/10.1002/2017WR021626>

622 Hannah, D.M., Demuth, S., van Lanen, H.A.J., Looser, U., Prudhomme, C., Rees, G., Stahl, K.,
623 Tallaksen, L.M., 2011. Large-scale river flow archives: Importance, current status and
624 future needs. *Hydrol. Process.* 25, 1191–1200. <https://doi.org/10.1002/hyp.7794>

625 Höfle, B., 2009. "Water Surface Mapping from Airborne Laser Scanning using Signal Intensity
626 and Elevation Data." *Earth Surface Processes and Landforms* 34 (12): 1635-1649.
627 [doi:10.1002/esp.1853](https://doi.org/10.1002/esp.1853).

628 Hudson, A.S., Talke, S.A., Branch, R., Chickadel, C., Farquharson, G., Jessup, A., 2017. Remote
629 measurements of tides and river slope using an airborne lidar instrument. *J. Atmos. Ocean.*
630 *Technol.* 34, 897–904. <https://doi.org/10.1175/JTECH-D-16-0197.1>

631 King, T. V., Neilson, B.T., Rasmussen, M.T., 2018. Estimating Discharge in Low-Order Rivers
632 with High-Resolution Aerial Imagery. *Water Resour. Res.* 54, 1–16.
633 <https://doi.org/10.1002/2017WR021868>

634 Kouraev, A. V., Zakharova, E.A., Samain, O., Mognard, N.M., Cazenave, A., 2004. Ob' river
635 discharge from TOPEX/Poseidon satellite altimetry (1992-2002). *Remote Sens. Environ.*
636 93, 238–245. <https://doi.org/10.1016/j.rse.2004.07.007>

637 Langhorst, T., T.M. Pavelsky, R.P.M. Frasson, R. Wei, A. Domeneghetti, E.H. Altenau, M.T.
638 Durand, J.T. Minear, K. Wegmann, and M. Fuller, In Review. Anticipated improvements to
639 in-river DEMs from the Surface Water and Ocean Topography mission, *Frontiers in Earth*
640 *Science*.

641 Maillard, P., Bercher, N., Calmant, S., 2015. New processing approaches on the retrieval of
642 water levels in Envisat and SARAL radar altimetry over rivers: A case study of the São
643 Francisco River, Brazil. *Remote Sens. Environ.* 156, 226–241.
644 <https://doi.org/10.1016/j.rse.2014.09.027>

645 Manning, R., Griffith, J. P., Pigot, T. F., & Vernon-Harcourt, L. F., 1890. On the flow of water in
646 open channels and pipes. *Transactions of the Institution of Civil Engineers of Ireland*.

647 McFeeters, S.K., 1996. The use of the Normalized Difference Water Index (NDWI) in the
648 delineation of open water features. *Int. J. Remote Sens.* 17, 1425–1432.
649 <https://doi.org/10.1080/01431169608948714>

650 Moller, D., Rodríguez, E., Carswell, J., Esteban-Fernandez, D., 2011. A calibration/validation
651 platform for the SWOT mission, in: *Proc. International Geoscience and Remote Sensing*
652 *Symposium*. Vancouver, Canada.

653 Neeck, S.P., Lindstrom, E.J., Vaze, P. V., Fu, L.-L., 2012. Surface Water and Ocean Topography
654 (SWOT) mission. *Proc. SPIE 8533, Sensors, Syst. Next-Generation Satell.* XVI 8533G.
655 <https://doi.org/10.1117/12.981151>

656 O’Loughlin, F., Trigg, M.A., Schumann, G.J.P., Bates, P.D., 2013. Hydraulic characterization of
657 the middle reach of the Congo River. *Water Resour. Res.* 49, 5059–5070.
658 <https://doi.org/10.1002/wrcr.20398>

659 O’Loughlin, F.E., Neal, J., Yamazaki, D., Bates, P.D., 2016. ICESat-derived inland water
660 surface spot heights. *Water Resour. Res.* 1–20. <https://doi.org/10.1002/2014WR015716>

661 Papa, F., Durand, F., Rossow, W.B., Rahman, A., Bala, S.K., 2010. Satellite altimeter-derived
662 monthly discharge of the Ganga-Brahmaputra River and its seasonal to interannual
663 variations from 1993 to 2008. *J. Geophys. Res. Ocean.* 115, 1–19.
664 <https://doi.org/10.1029/2009JC006075>

665 Paris, A., Paiva, R.C.D., Silva, J.S., Moreira, D.M., Calmant, S., Garambois, P.-A., Collischonn,
666 W., Bonnet, M.P., Seyler, F., 2016. Stage-discharge rating curves based on satellite
667 altimetry and modeled discharge in the Amazon basin. *Water Resour. Res.* 1–20.
668 <https://doi.org/10.1002/2014WR015716>

669 Pavelsky, T.M., Durand, M.T., Andreadis, K.M., Beighley, R.E., Paiva, R.C.D., Allen, G.H.,
670 Miller, Z.F., 2014. Assessing the potential global extent of SWOT river discharge
671 observations. *J. Hydrol.* 519, 1516–1525. <https://doi.org/10.1016/j.jhydrol.2014.08.044>

672 Pitcher, L.H., Pavelsky, T.M., Smith, L.C., Moller, D.K., Altenau, E.H., Allen, G.H., Lion, C.,
673 Butman, D., Cooley, S.W., Fayne, J. and Bertram, M., 2018. AirSWOT InSAR mapping of
674 surface water elevations and hydraulic gradients across the Yukon Flats Basin, Alaska.
675 *Water Resources Research*.

676 Rodriguez, E., 2016. Surface Water and Ocean Topography Mission (SWOT) Project - Science
677 Requirements Documents, SWOT NASA/JPL Project.

678 Rodriguez, E., Martin, J.M., 1992. Theory and design of interferometric synthetic aperture
679 radars. *IEE Proc. F Radar Signal Process.* 139, 147. [https://doi.org/10.1049/ip-f-](https://doi.org/10.1049/ip-f-2.1992.0018)
680 [2.1992.0018](https://doi.org/10.1049/ip-f-2.1992.0018)

681 Rosen, P.A., Hensley, S., Joughin, I.R., Li, F.K., Madsen, S.N., Rodriguez, E., Goldstein, R.M.,
682 2000. Synthetic aperture radar interferometry Synthetic aperture radar interferometry. *Proc.*
683 *IEEE* 88, 333–382. <https://doi.org/10.1088/0266-5611/14/4/001>

684 Sanders, B.F., 2007. Evaluation of on-line DEMs for flood inundation modeling. *Adv. Water*
685 *Resour.* 30, 1831–1843. <https://doi.org/10.1016/j.advwatres.2007.02.005>

686 Schumann, G., Matgen, P., Cutler, M.E.J., Black, A., Hoffmann, L., Pfister, L., 2008.
687 Comparison of remotely sensed water stages from LiDAR, topographic contours and
688 SRTM. *ISPRS J. Photogramm. Remote Sens.* 63, 283–296.
689 <https://doi.org/10.1016/j.isprsjprs.2007.09.004>

690 Smith, J.S., Chandler, J., Rose, J., 2009. High spatial resolution data acquisition for the
691 geosciences: kite aerial photography. *Earth Surf. Process. Landforms* 34, 155–161.
692 <https://doi.org/10.1002/esp>

693 Smith, L.C., 1997. SATELLITE REMOTE SENSING OF RIVER INUNDATION AREA ,
694 STAGE , AND DISCHARGE : A REVIEW. *Hydrol. Process.* 11, 1427–1439.
695 Tourian, M.J., Tarpanelli, A., Elmi, O., Qin, T., Brocca, L., Moramarco, T., Sneeuw, N., 2016.
696 Spatiotemporal densification of river water level time series by multimission satellite
697 altimetry. *Water Resour. Res.* 52, 1140–1159. <https://doi.org/10.1002/2015WR017654>
698
699
700
701
702
703
704
705
706
707
708
709
710
711
712
713
714
715
716
717
718
719
720
721
722
723
724
725
726
727
728
729
730
731
732
733
734
735
736
737
738

739 **TABLES:**

740

741 Table 1: Root-mean-square differences (RMSDs) and bias between the AirSWOT and pressure
 742 transducer same-day water surface elevations (WSEs) and along-flow slopes.

Date	WSE RMSD (cm)	Mean WSE Bias (cm)	WSE RMSD, Bias removed (cm)	Slope RMSD (cm/km)
June 7	18.2	-14.6	10.8	1.4
June 9	17.2	-8.1	15.0	1.8
June 16	24.2	-20.7	11.1	1.8
June 17	12.5	-9.3	8.3	1.6
June 18	19.3	-15.4	11.6	1.7
June 22	19.2	-13.3	12.7	1.2
All Days	18.8	-13.6	11.8	1.6

743

744

745 Table 2: Manning’s equation parameters for each pressure transducer cross section.

Pressure Transducer	Width Range (m)	Number of Channels in Cross Section	Manning’s n Range
1	468-654	5	0.065-0.095
2	413-458	4	0.055-0.080
3	321-326	1	0.045-0.055
4	468-616	6	0.055-0.085
5	462-619	6	0.045-0.080
6	354-458	4	0.045-0.070
8	267-305	2	0.035-0.055
9	209-258	2	0.025-0.035
11	297-382	2	0.035-0.065
12	259-279	1	0.035-0.045

746

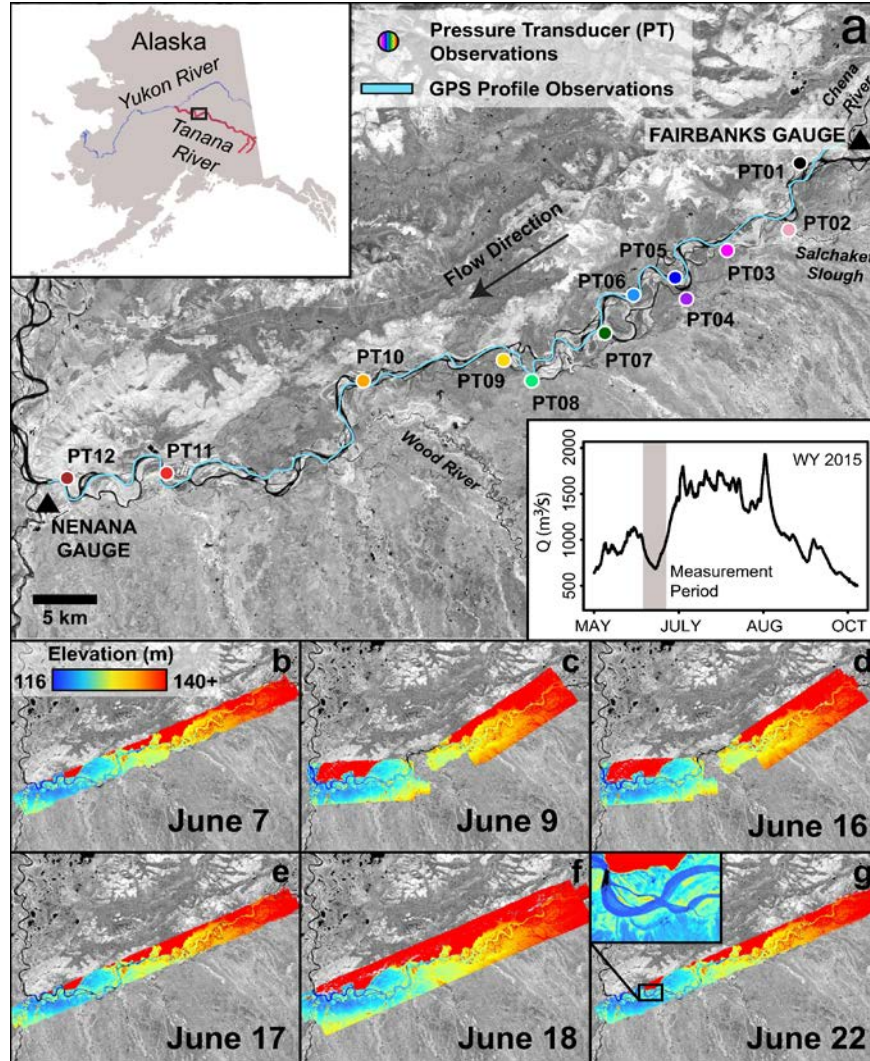
747

748 Table 3: Root-mean-square differences (RMSDs) between AirSWOT and pressure transducer
 749 discharge estimates.

Date	RMSD (m³/s)	RMSD (%)
June 7	105.8	11.1
June 9	148.1	18.0
June 16	107.9	15.6
June 17	85.4	11.9
June 18	98.6	12.6
June 22	117.9	12.6
All Days	112.3	13.8

750

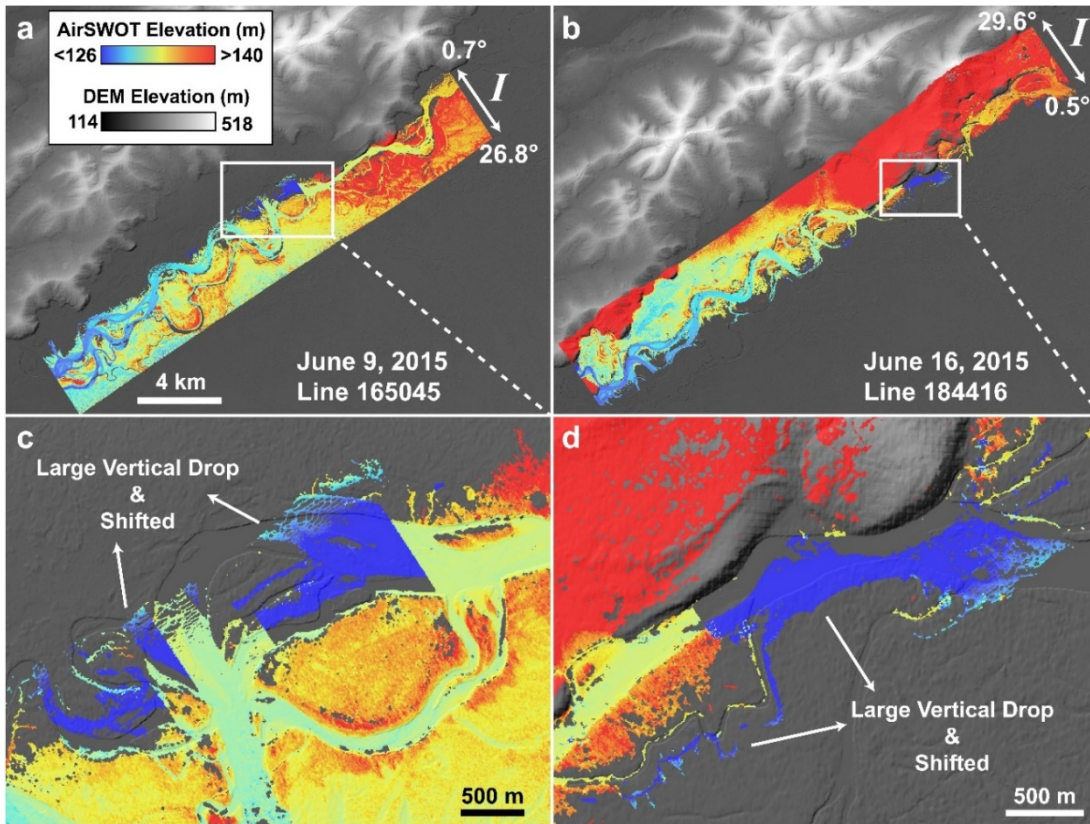
751 FIGURES:
752



753

754 Fig. 1: a) Tanana River study reach depicted with a Landsat 8 near-infrared image acquired on
755 June 15, 2015. Pressure transducer (PT) locations are indicated by the different colored circles
756 and GPS profile measurements are indicated by the light blue line. Upper left inset displays the
757 study reach location within the state of Alaska. Lower right inset displays the Nenana gauge
758 hydrograph during the open water season for the 2015 water year (WY). The grey shaded area
759 within the hydrograph shows the timeframe of the field campaign. b-g) AirSWOT extent and
760 elevation mosaics for the six different flights.

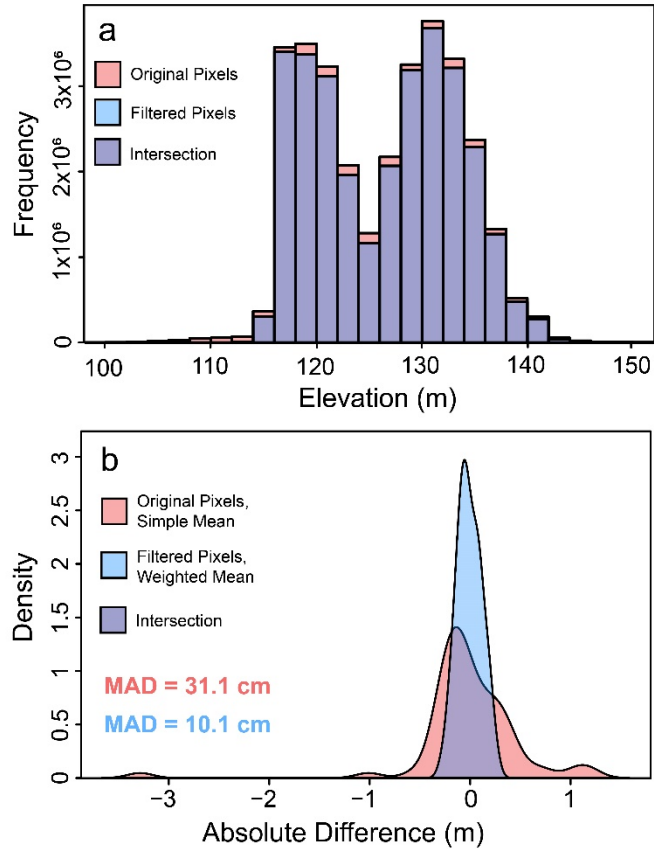
761



762

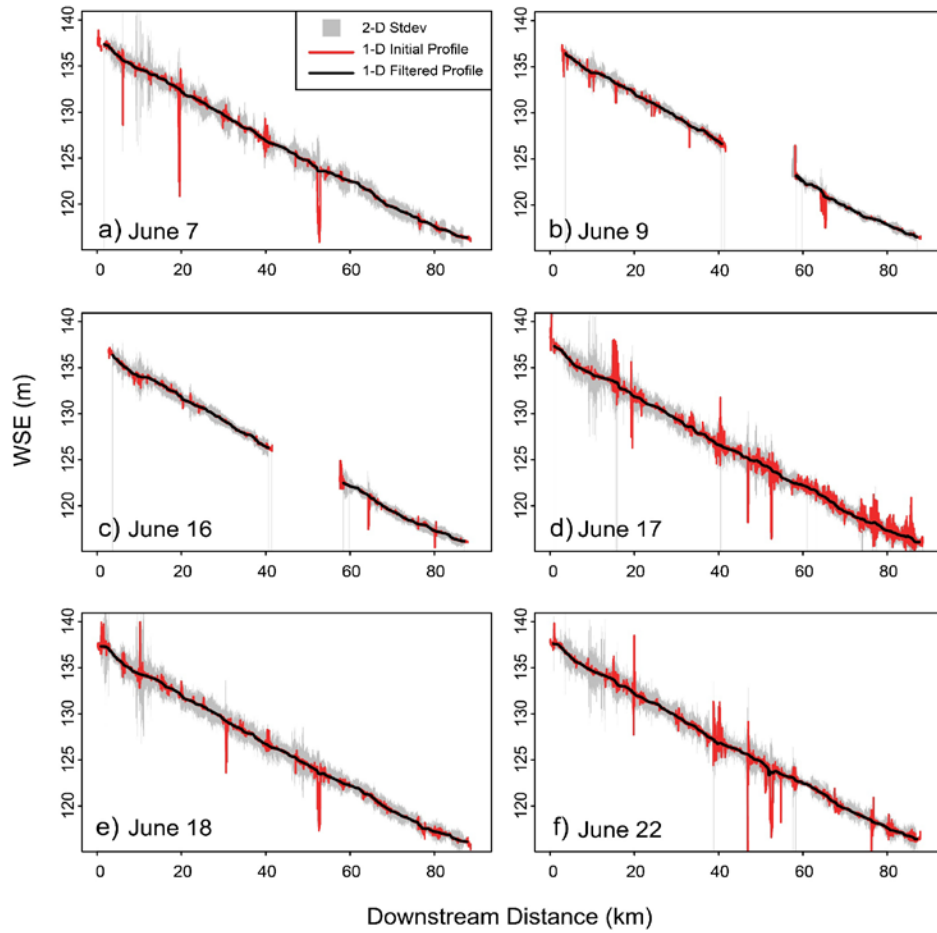
763 Fig. 2: Examples of ambiguity height errors in two AirSWOT lines from June 9, 2015 and June
 764 16, 2015. The areas of dark blue pixels, which designate significant vertical drops and
 765 geolocation errors, are manually removed.

766
 767
 768
 769
 770
 771
 772
 773
 774
 775
 776
 777
 778
 779
 780
 781
 782
 783
 784



785
 786 Fig 3: (a) Histograms of the AirSWOT WSE pixels from all six flight collections before (red)
 787 and after (blue) the 2-D spatial filtering. (b) Density plots of the absolute differences between the
 788 spatially-averaged AirSWOT and PT WSEs with (blue) and without (red) the 2-D filtering and
 789 weighted mean calculation. Mean absolute difference (MAD) values for each method are shown.

790
 791
 792
 793
 794
 795
 796
 797
 798
 799
 800
 801
 802
 803
 804
 805



806

807 Fig. 4: AirSWOT river water surface elevation (WSE) profiles. The initial 1-D AirSWOT
 808 profiles (red) are produced by calculating a weighted mean of the 2-D AirSWOT pixels. Severe
 809 peaks in the initial 1-D profiles are removed using a running median filter with a window size of
 810 500 observations (~1600 m) to yield the final profiles (black). The final profiles are used to
 811 calculate river surface slopes and slope changes. Standard deviations (Stdev) for the 2-D
 812 AirSWOT pixels measured across the orthogonal at each GPS profile observation are shown in
 813 grey.

814

815

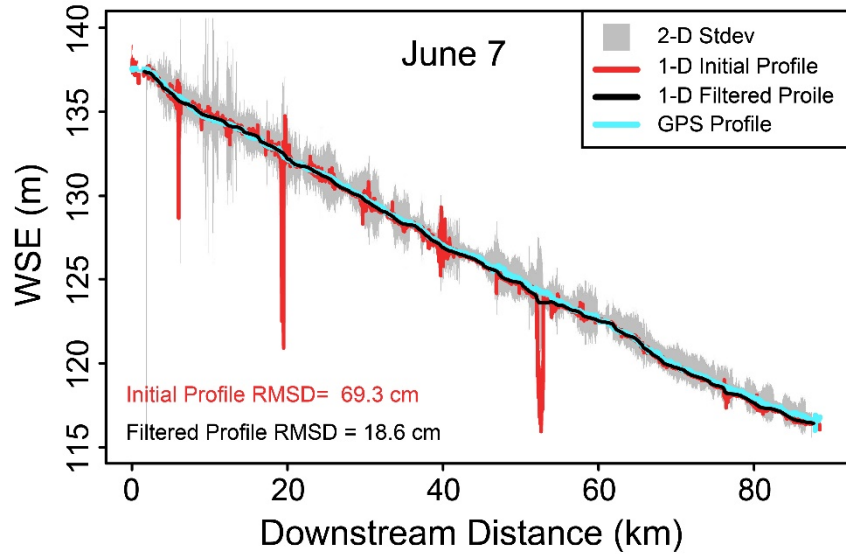
816

817

818

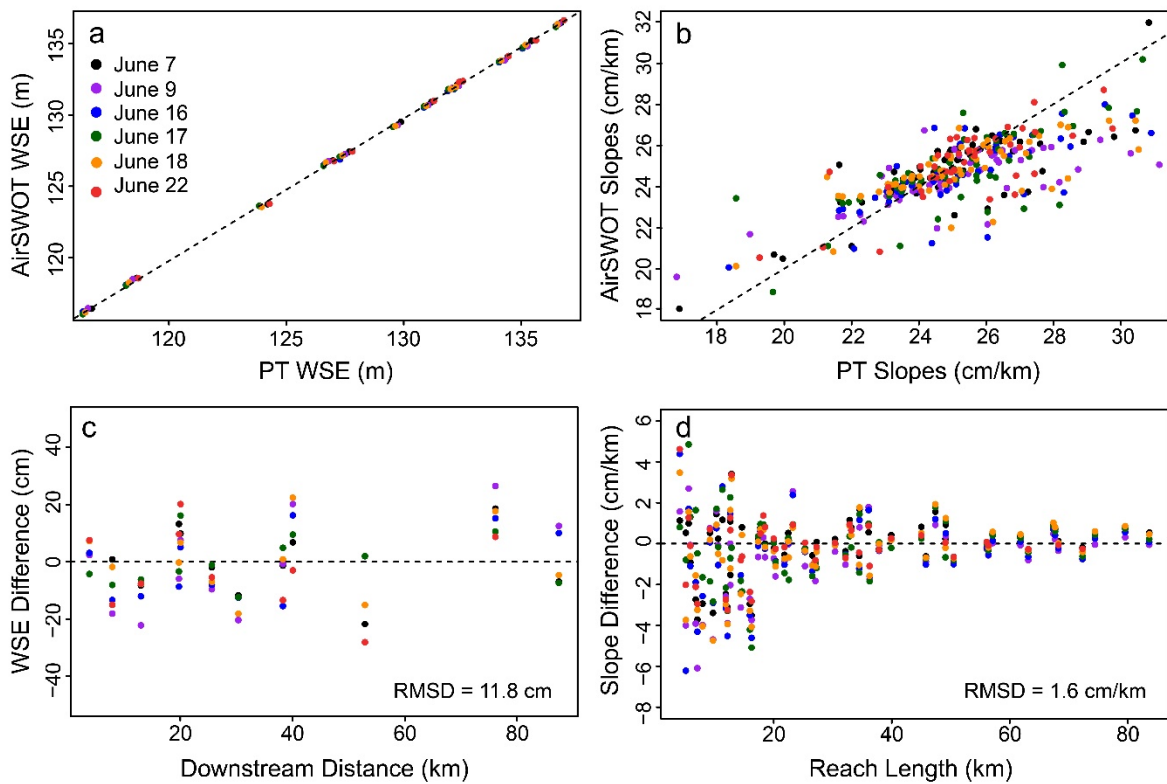
819

820



821
 822 Fig. 5: AirSWOT water surface elevation (WSE) profile versus GPS profile on June 7, 2015.
 823 Standard deviations of the 2-D AirSWOT pixels across the orthogonal at each GPS profile
 824 observation are shown in grey. The final 1-D AirSWOT profiles (black) are created using a
 825 running-median filter with a window size of 500 observations (~1600 m) along the initial
 826 profiles (red). Root mean square differences (RMSD) between the two AirSWOT profiles and
 827 GPS profile (blue) are displayed.

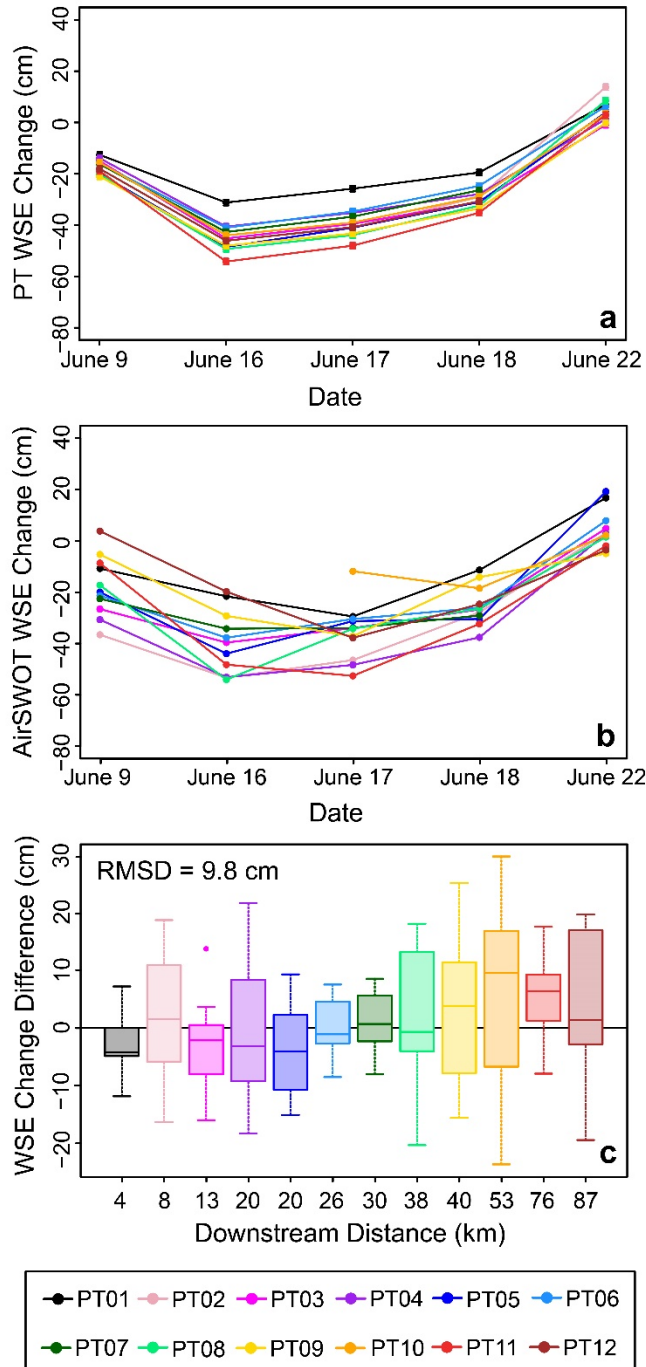
828
 829
 830
 831
 832
 833
 834
 835
 836
 837
 838
 839
 840
 841
 842
 843
 844
 845
 846
 847



848

849 Fig. 6: AirSWOT vs. pressure transducer (PT) WSEs (a) and slopes (b). Dashed diagonal lines
 850 indicate the 1:1 lines. AirSWOT WSE (c) and slope (d) differences compared to the PTs for the
 851 various AirSWOT collections. AirSWOT WSEs and WSE differences are shown with the daily
 852 mean biases removed. Dashed horizontal lines indicate zero height and slope differences.

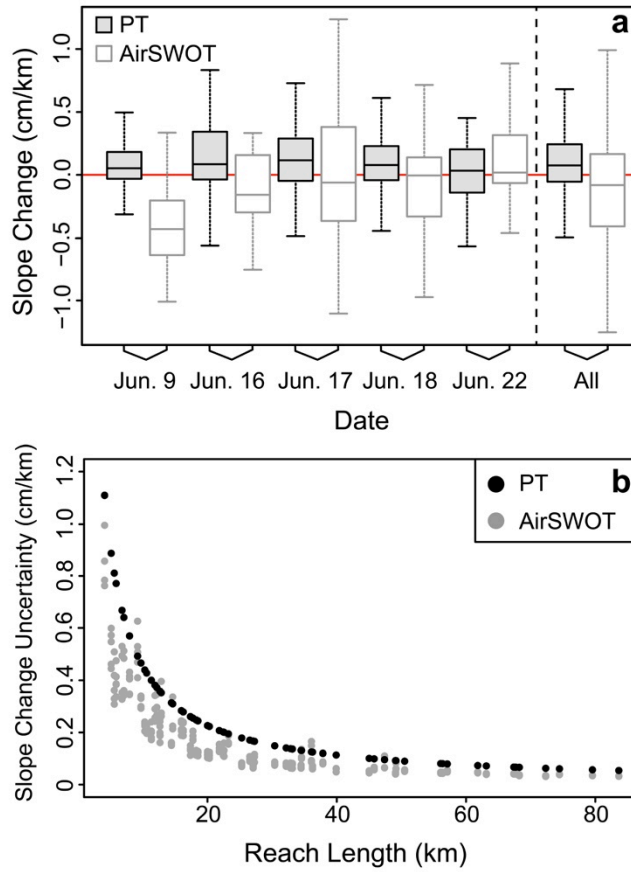
853



854

855 Fig. 7: Pressure transducer (PT) (a) and AirSWOT (b) WSE changes between June 7th and all
 856 subsequent dates (n = 58). c) AirSWOT WSE change differences at each PT location for all
 857 possible date combinations (n = 161). All AirSWOT WSE changes are calculated with the bias-
 858 corrected WSEs. Different colors represent the various PT locations. PT uncertainty bars are too
 859 small to visualize.

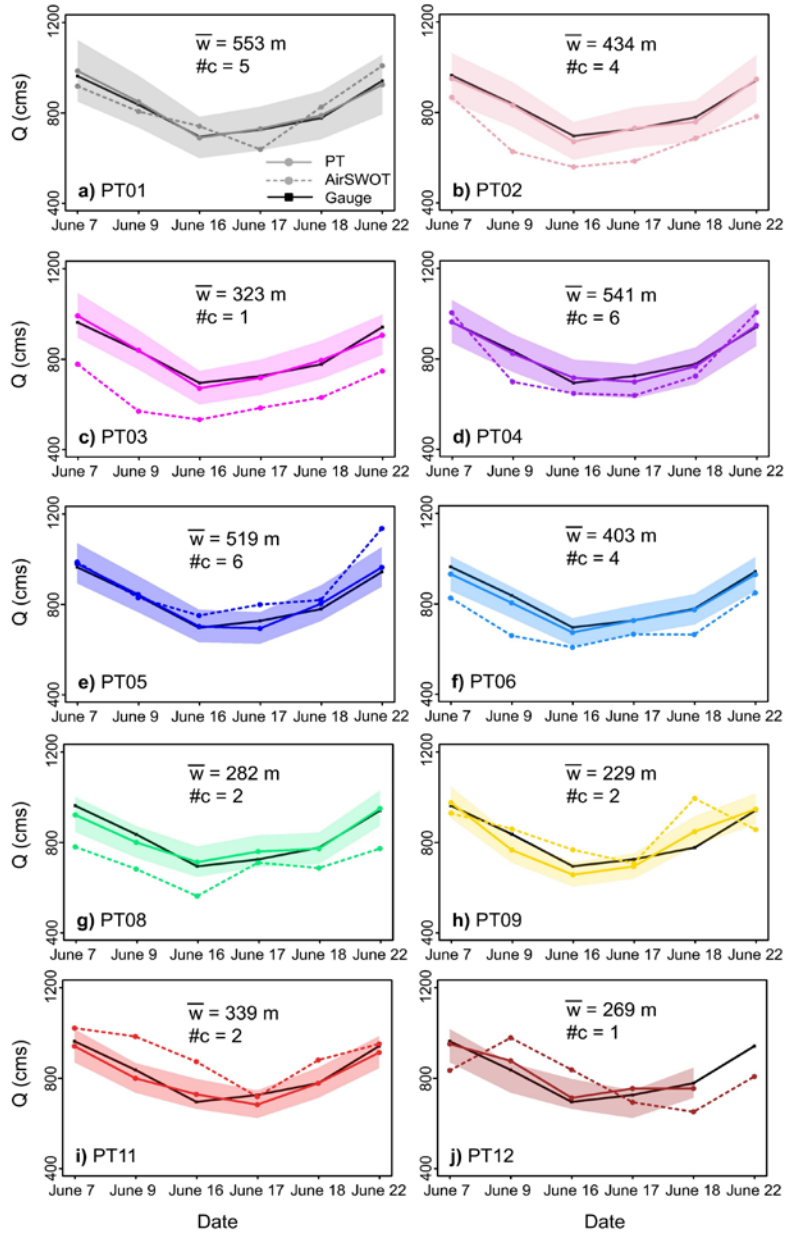
860



861

862 Fig. 8: a) Boxplots of observed slope changes by the pressure transducers (PT, grey) and
 863 AirSWOT (white) between June 7th and all subsequent dates ($n = 297$), as well as possible
 864 date combinations (All) ($n = 766$). Outliers make up 15% of the data points and are not shown in
 865 the boxplots of slope change distributions. The red horizontal line designates zero slope change,
 866 while the black vertical dashed line separates the consecutive slope change distributions from the
 867 distributions for all possible date combinations. b) AirSWOT (grey) and PT (black) slope change
 868 uncertainties versus reach length.

869
 870
 871
 872
 873
 874
 875
 876
 877
 878
 879

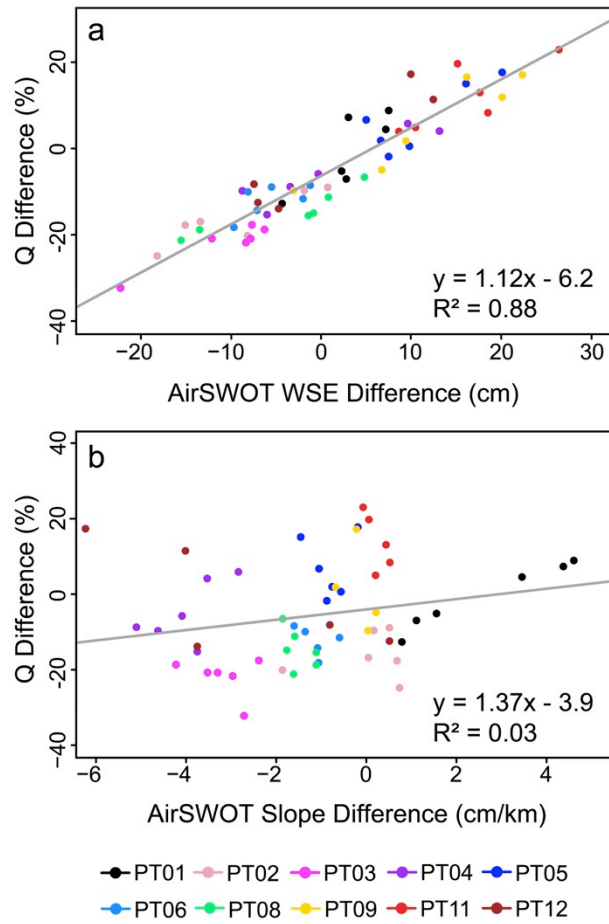


880

881 Fig. 9: Tanana River discharge estimates calculated using Manning's equation. Solid colored
 882 lines display discharge estimates using the PT WSEs and slopes, while dashed colored lines
 883 display discharge estimates using AirSWOT WSEs and slopes. Shaded colored areas indicate the
 884 PT discharge uncertainties. Nenana gauge discharge is shown as the black solid line in each
 885 panel. Average width (\bar{w}), and number of channels in the cross section ($\#c$) are displayed.

886
 887
 888
 889
 890
 891
 892

893



894

895 Fig. 10: The differences between AirSWOT and PT observations of WSEs (a) and
896 versus differences in calculated discharge values when using AirSWOT observations versus PT
897 observations of WSE and slope. Colored dots represent the different pressure transducer (PT)
898 locations.

899